Periodic table screening for enhanced positive contrast in MRI and *in vivo* uptake in glioblastoma

Aitor Herraiz, M. Puerto Morales, Lydia Martínez-Parra, Nuria Arias-Ramos, Pilar López-Larrubia, Lucía Gutiérrez, Jesús Mejías, Carlos Díaz-Ufano Jesús Ruiz-Cabello, Fernando Herranz.*

SUPPORTING INFORMATION

Structural and compositional evaluation.

The synthesized nanoparticles were characterized by dynamic light scattering (DLS) using a Zetasizer Nano ZS90 (Malvern Panalytical, UK) to assess both the hydrodynamic size and Z-potential of the nanoparticles. For any nanoparticle that we obtained, we considered meeting the necessary conditions if they showed a negative potential of approximately − 30 mV with a hydrodynamic size of approximately 10 nm. The exact composition was analyzed by inductively coupled plasma-optical emission spectrometry (ICP-OES) using an Optima 2100 DV PerkinElmer equipment. The samples were digested with a HNO_3:HCl (1:1) mixture for at least 24 h at room temperature and diluted to a controlled volume. For Fourier transform infrared spectroscopy (FTIR), freeze-dried samples were compacted in KBr tablets and measured using a Bruker Vertex 70V spectrophotometer (2 cm^{-1} resolution). The external organic layer was then analyzed by thermogravimetric analysis (TGA). Between 5-10 mg of freeze-dried sample was heated in a controlled manner (10 °C/min from 10 °C to 900 °C under an oxygen atmosphere) in a thermogravimetric analyzer (SDT Q600 V20.9 Build

20). After humidity correction, the organic coating was estimated as a percentage of the mass loss.

X-ray diffraction (XRD)

The crystal structure patterns of the freeze-dried samples were acquired via X-ray diffraction (XRD) using a Bruker D8 Advance powder diffractometer with Cu Kα radiation and an energy discriminator. The acquisitions were performed on fine powders pressed on a 32 mm low background silicon single crystal sample holder in the 2θ range [10°–70°] with an angular step of 0.04°. The pattern was analyzed to accurately evaluate the position and width of the peaks. Scherrer equation was used to determine the crystal size of the M-IONP considering instrumental broadening.

Transmission electron microscopy (TEM).

Nanoparticle size and distribution were analyzed by transmission electron microscopy

(TEM. JEOL JEM 1010). The mean size and deviation were determined by measuring ~150 particles using the ImageJ digital software and fitting the data to a log-normal curve.

High-angle annular dark-field scanning transmission electron microscopy (HADDF-STEM).

The samples were prepared by placing a drop of a dilute MNP suspension on a carbon-coated copper grid and allowing it to dry. Imaging with a high-angle annular dark-field detector (STEM-HAADF) was performed using an Analytical Titan (FEI) microscope with an accelerating voltage of 300 keV.

Energy-dispersive X-ray spectroscopy (EDS) was performed using the same instrument that has also installed a EDS Oxford Instruments Ultim Max TLE 100 spectrometer to evaluate the chemical composition of the particles. The presence of Iron, Gallium and Zinc was studied in all the samples at the characteristic x-ray energies (Fe: Kα 6.398 keV & Lα 0.705 keV; Ga: Kα 9.241 keV & Lα 1.098 keV; Zn: Kα 8.630 keV & Lα 1.012 keV). In addition, signal coming from the Copper grid was also detected (Cu Kα 8.040 keV, K_β 8.91keV).

Multivariate data analysis

In this study, we employed multivariate methods to investigate the impact of various ions on the magnetic and structural characteristics of hybrid nanoparticles doped with diverse metals. Analyses were conducted using GraphPad Prism version 10 for multivariate statistical analysis and data visualization.

Two primary multivariate techniques, Principal Component Analysis (PCA) and Pearson Correlation Analysis, were used to extract meaningful insights from our dataset. These methods allowed us to explore the complex interrelationships among multiple variables of the study (theoretical concentration, metal incorporation, metal/concentration ratio of iron, crystal size, hydrodynamic size, zeta potential value, % coating measured by TGA, M_{SAT}, r_1, and r_2), shedding light on how different ions and metal (grouped by valence) dopants influence the properties of different hybrid nanoparticles.

Principal Component Analysis (PCA) is a dimensionality reduction technique that transforms the original variables into a set of uncorrelated variables/principal components. PCA helps to identify patterns and trends within the data by highlighting the most significant sources of variation. In our study, PCA was instrumental in reducing the dimensionality of our dataset while preserving the

critical information required to discern the effects of various ions and metal dopants on the properties of the nanoparticles.

Pearson's Correlation Analysis, on the other hand, measures the strength and direction of the linear relationships between pairs of variables. By calculating the Pearson correlation coefficients of these variables, we assessed the degree of association between different ions and the relaxometric/magnetic/structural properties of the nanoparticles. This analysis allowed us to identify statistically significant correlations, helping us uncover potential causal links between specific ions and observed changes in the characteristics of the nanoparticles.

Metal	Metal Source	Added Conc. (mM)	Incorporation (%)	Ratio [mM] [M]/[Fe]	Crystal Size (Å)	Hydrodynamic size (nm)	$Z_{pot.}$ (mV)	% coating	M_{SAT} (Am^2/kg)	r_1 ($mM^{-1}s^{-1}$)	r_2 ($mM^{-1}s^{-1}$)	r_2/r_1
IONP		-	-	-	50.4	7.59	-27.4	26.50	92.67	12.8 ± 1.6	27.3 ± 4.3	2.1
Be^{2+}	Beryllium (II) sulphate tetrahydrate	4.5	21.15	0.042	33.4	7.10	-33.7	28.26	73.18	7.6	14.3	1.9
Mg^{2+}	Magnesium (II)chloride hexahydrate	1.5	10.29	0.006	41.4	10.85	-27.5	25.06	87.89	13.6	26.8	2.0
Mg^{2+}		4.5	9.46	0.015	35.5	9.06	-26.6	-	-	11.6	29.2	2.5
Mg^{2+}		7.0	9.55	0.028	40.5	13.88	-21.0	-	-	13.3	31.6	2.4
Mg^{2+}		10.0	7.71	0.032	37.6	15.46	-23.9	-	-	12.2	29.4	2.4
Al^{3+}	Aluminium (III)chloride	4.5	53.81	0.117	35.4	6.57	-32.2	-	-	6.5	13.4	2.0
Ca^{2+}	Calcium chloride hydrate	1.5	78.60	0.048	37.4	7.78	-23.2	24.20	86.48	12.4	25.8	2.1
Ca^{2+}		4.5	42.94	0.070	34.3	6.37	-27.8	23.08	84.19	12.4	23.9	1.9
Ca^{2+}		7.0	22.63	0.077	35.4	8.57	-29.6	-	-	11.8	24.2	2.0
Ca^{2+}		10.0	19.65	0.095	36.6	8.27	-24.9	-	-	14.6	28.9	2.0
Sc^{3+}	Scandium (III) chloride hydrate	4.5	20.82	0.033	40.1	8.30	-22.1	28.58	80.98	12.1	25.7	2.1
Cr^{3+}	Chromium (III) chloride hexahydrate	4.5	31.48	0.067	49.3	6.78	-39.2	30.96	46.84	4.7	10.0	2.1
Mn^{2+}	Manganese (II) chloride tetrahydrate	4.5	43.98	0.085	38.9	7.41	-24.6	33.15	82.06	11.2	25.4	2.3
Ni^{2+}	Nickel (II) chloride hexahydrate	1.5	17.04	0.010	40.8	13.39	-30.0	-	-	11.6	26.5	2.3
Ni^{2+}		4.5	13.37	0.025	45.5	6.10	-22.7	22.98	75.52	11.2	22.1	2.0
Ni^{2+}		7.0	14.85	0.045	39.1	9.11	-26.8	-	-	11.4	23.4	2.0
Ni^{2+}		10.0	14.57	0.054	38.4	8.64	-29.3	-	-	9.7	21.6	2.2
Co^{2+}	Cobalt (II) chloride hexahydrate	4.5	22.45	0.052	36.8	8.08	-33.1	27.10	85.22	11.9	25.0	2.1
Cu^{2+}	Copper (II) chloride	4.5	-	-	-	-	-	-	-	-	-	-
Zn^{2+}	Zinc (II) chloride	1.5	97.12	0.058	37.0	6.64	-33.40	25.23	98.48	17.4 ± 0.6	33.8 ± 2.3	1.9
Zn^{2+}		4.5	99.71	0.163	42.6	8.30	-22.10	28.46	107.52	12.0	24.1	2.0
Zn^{2+}		7.0	75.66	0.205	36.1	6.29	-32.37	22.90	66.05	8.1	14.8	1.8
Zn^{2+}		10.0	89.67	0.326	41.1	5.71	-24.53	22.14	64.38	1.5	3.1	2.1

Ga^{3+}		1.5	49.72	0.035	50.2	8.52	-31.07	24.52	85.73	17.4 ± 0.8	38.6 ± 4.7	2.2
Ga^{3+}	Gallium (III)	4.5	52.58	0.092	49.4	8.28	-30.10	24.91	96.88	16.9	36.3	2.1
Ga^{3+}	nitrate hydrate	7.0	50.20	0.151	45.8	8.91	-35.03	18.64	64.65	14.4	31.0	2.2
Ga^{3+}		10.0	49.12	0.200	50.1	9.42	-34.97	22.83	68.51	12.0	29.4	2.5
Sr^{2+}	Strontium	1.5	34.81	0.025	38.0	8.74	-38.70	26.55	80.55	15.3	30.1	2.0
Sr^{2+}	chloride anhydrous	4.5	19.38	0.041	37.0	6.36	-31.50	27.83	88.87	14.3	30.3	2.1
Y^{3+}	Yttrium (III) chloride hexahydrate	4.5	26.54	0.069	37.2	6.11	-28.00	44.44	52.51	4.8	10.1	2.1
Zr^{4+}	Zirconyl (IV) chloride octahydrate	4.5	76.38	0.131	36.2	8.60	-44.33	28.46	62.71	8.0	19.3	2.4
Mo^{3+}	Molybdenum (III) chloride	4.5	3.39	0.007	39.5	7.01	-29.33	31.89	78.40	9.9	19.6	2.0
Ru^{3+}	Ruthenium (III) chloride hexahydrate	-	-	-	-	-	-	-	-	-	-	-
Rh^{3+}	Rhodium (III) chloride hydrate	-	-	-	-	-	-	-	-	-	-	-
Pd^{2+}	Palladium (II) chloride	-	-	-	-	-	-	-	-	-	-	-
Ag^{+}	Silver (I) chloride	-	-	-	-	-	-	-	-	-	-	-
Cd^{2+}	Cadmium (II) chloride	4.5	14.31	0.026	49.2	7.27	-34.73	25.71	80.00	12.0	22.7	1.9
In^{3+}	Indium (III) chloride	-	-	-	-	-	-	-	-	-	-	-
Ba^{2+}	Barium (II)	1.5	34.22	0.022	41.1	7.79	-24.70	-	-	12.3	24.0	2.0
Ba^{2+}	sulphate	4.5	22.82	0.051	44.3	7.72	-28.00	23.33	63.27	10.9	22.5	2.1
La^{3+}	Lanthanum (III) chloride hydrate	1.5	41.16	0.037	49.6	5.59	-39.10	38.62	36.15	2.1	4.6	2.2
Ce^{3+}	Cerium (III) chloride	1.5	66.73	0.068	53.2	4.04	-32.00	47.27	16.24	0.4	0.8	1.9
Pr^{3+}	Praseodymium (III) chloride	-	-	-	-	-	-	-	-	-	-	-
Nd^{3+}	Neodymium (III) chloride hexahydrate	-	-	-	-	-	-	-	-	-	-	-
	Samarium (III)											

	chloride hexahydrate											
Eu^{3+}	Europium (III) chloride hexahydrate	1.5	51.22	0.040	32.8	6.59	-35.27	27.69	72.63	3.4	7.9	2.3
Gd^{3+}	Gadolinium (III) chloride hexahydrate	1.5	59.25	0.051	32.5	4.89	-41.50	30.72	32.46	2.5	4.7	1.9
Tb^{3+}	Terbium (III) chloride hexahydrate	4.5	40.77	0.098	38.9	6.13	-39.10	42.56	39.13	1.8	3.7	2.1
Dy^{3+}	Dysprosium (III) chloride hexahydrate	4.5	40.57	0.094	43.2	5.42	-36.97	38.40	39.83	2.1	4.2	2.0
Ho^{3+}	Holmium (III) chloride hexahydrate	4.5	30.72	0.071	33.8	6.56	-38.27	32.15	38.12	4.1	8.3	2.0
Er^{3+}	Erbium (III) chloride hexahydrate	4.5	31.23	0.071	33.7	6.34	-37.50	27.42	39.28	4.0	8.0	2.0
Tm^{3+}	Thulium (III) chloride	4.5	30.46	0.066	34.6	6.85	-25.87	35.15	53.82	6.2	12.6	2.0
Yb^{3+}	Ytterbium (III) chloride hexahydrate	4.5	40.81	0.077	38.2	6.19	-36.67	27.98	52.07	5.7	11.4	2.0
Lu^{3+}	Lutetium (III) chloride hexahydrate	4.5	32.71	0.078	36.0	8.54	-33.80	33.70	56.80	8.2	16.8	2.0
Hf^{4+}	Hafnium (IV) chloride	4.5	46.38	0.088	38.4	10.32	-36.53	27.40	68.43	12.9	30.1	2.3
W^{5+}	Tungsten (VI) chloride	-	-	-	-	-	-	-	-	-	-	-
Pt^{5+}	Platinum (IC) chloride	-	-	-	-	-	-	-	-	-	-	-
Au^{3+}	Gold (III) chloride hexahydrate	-	-	-	-	-	-	-	-	-	-	-

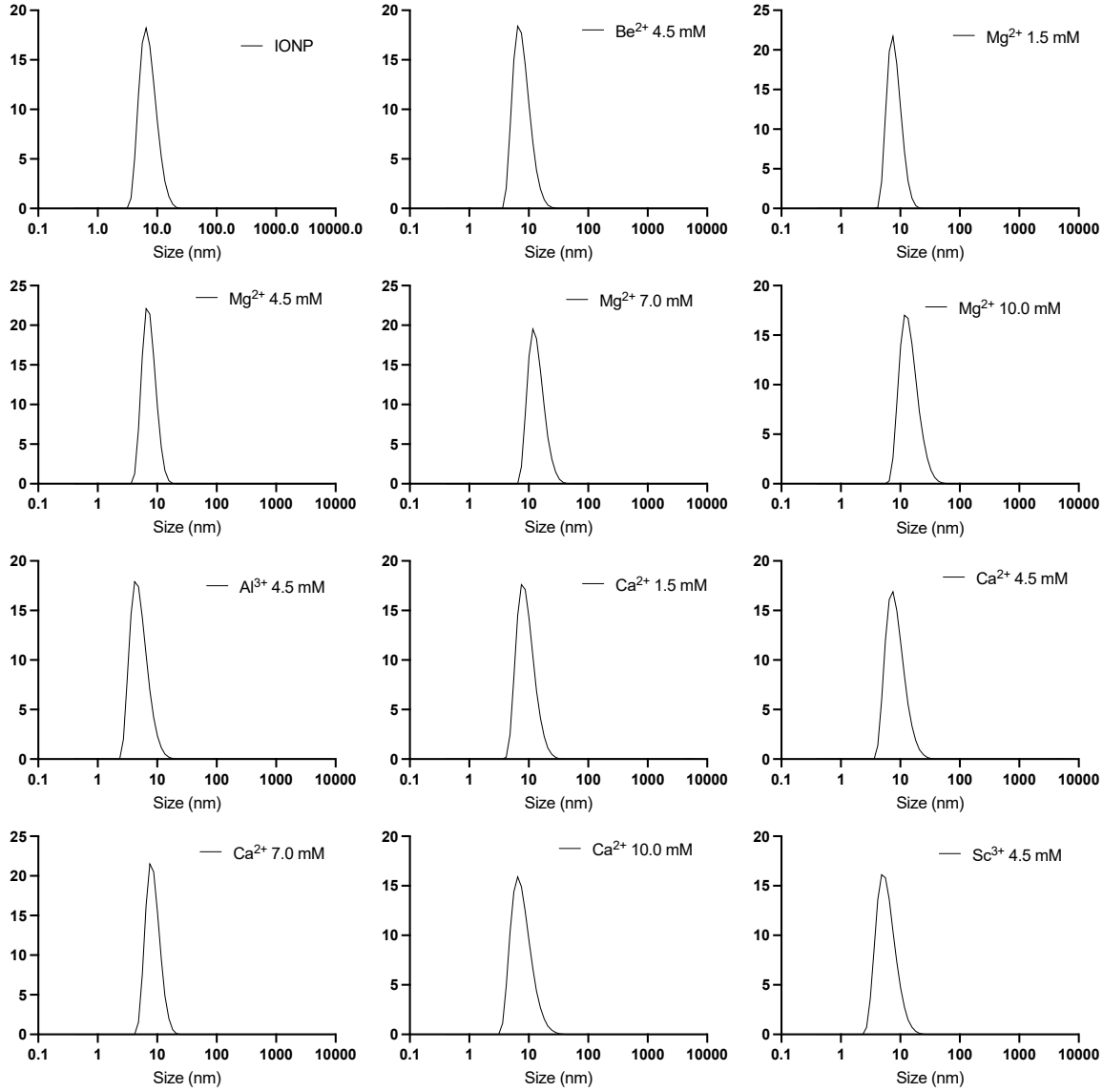

Figure S1. Hydrodynamic size distribution, measured by dynamic light scattering (DLS), of metal-doped IONP.

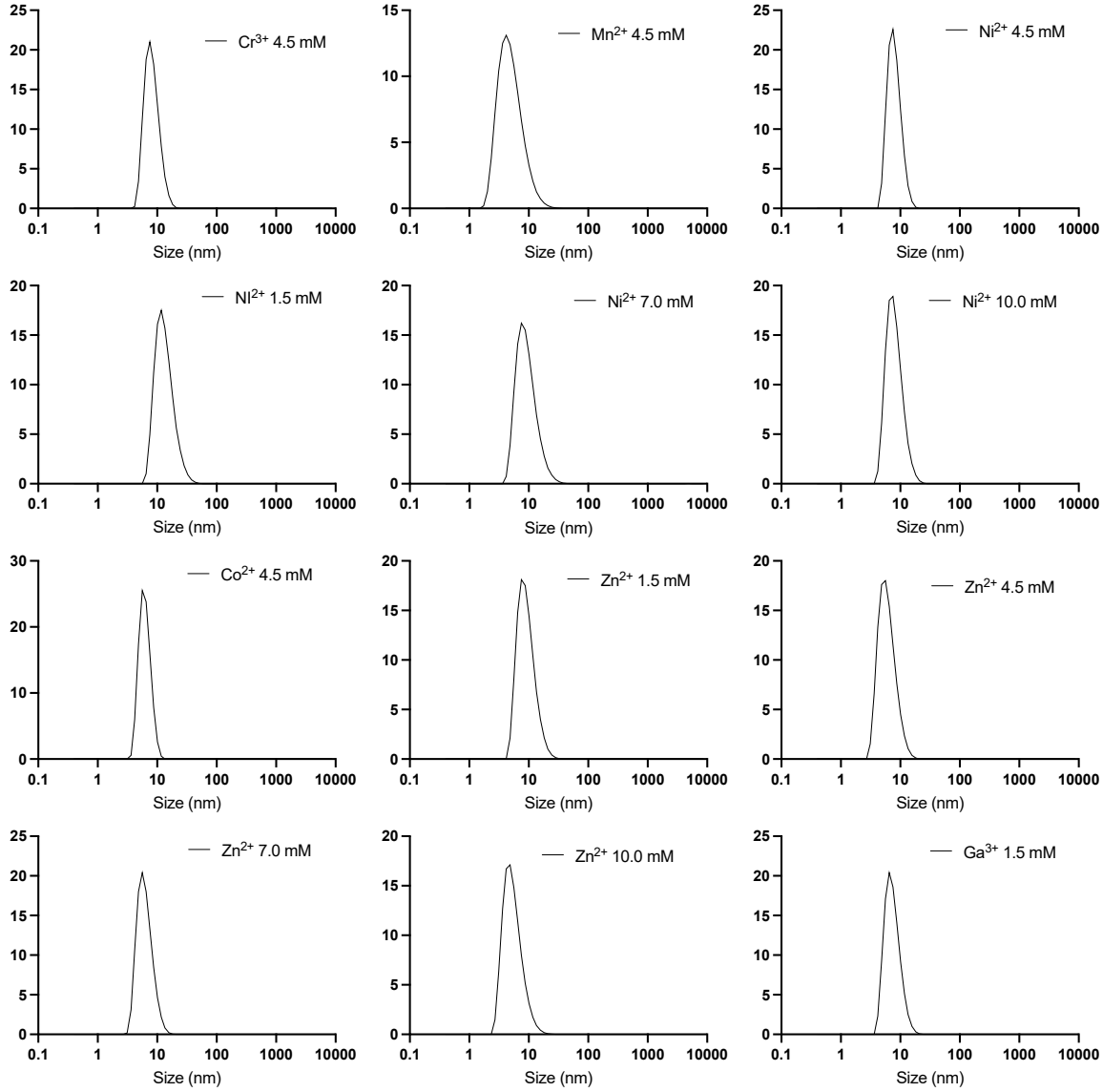

Figure S1. (Cont.)

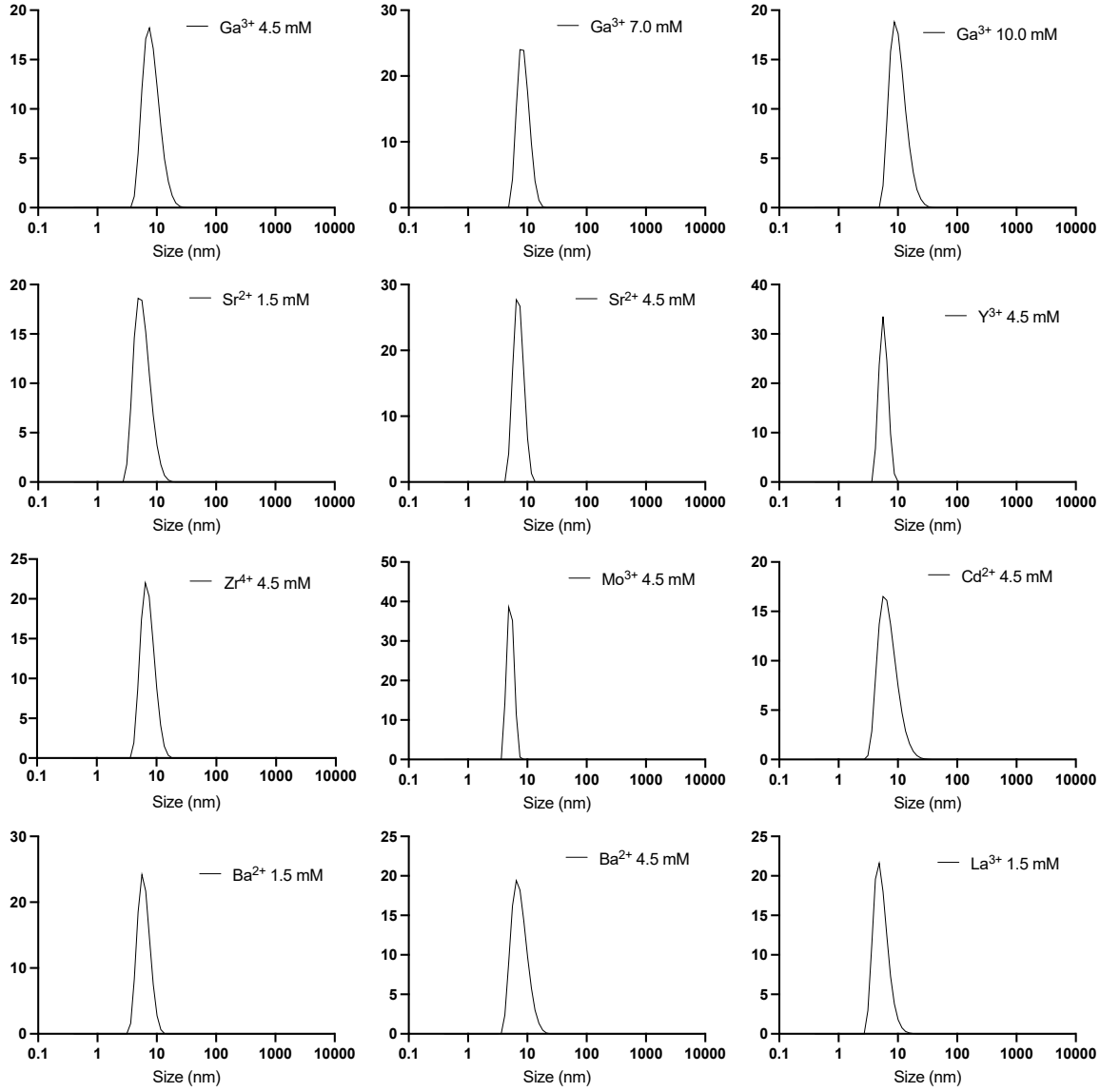

Figure S1. (Cont.)

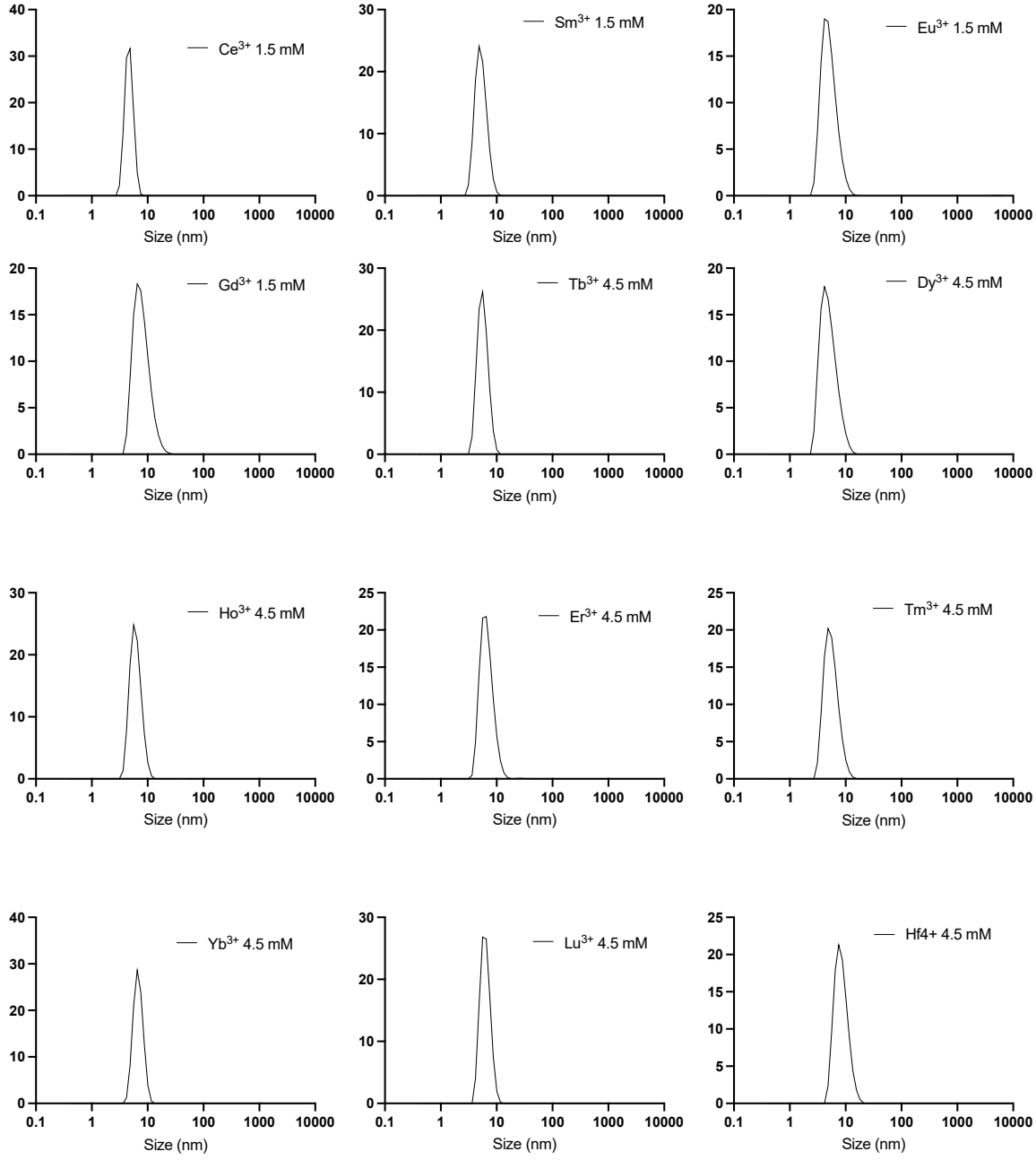

Figure S1. (Cont.)

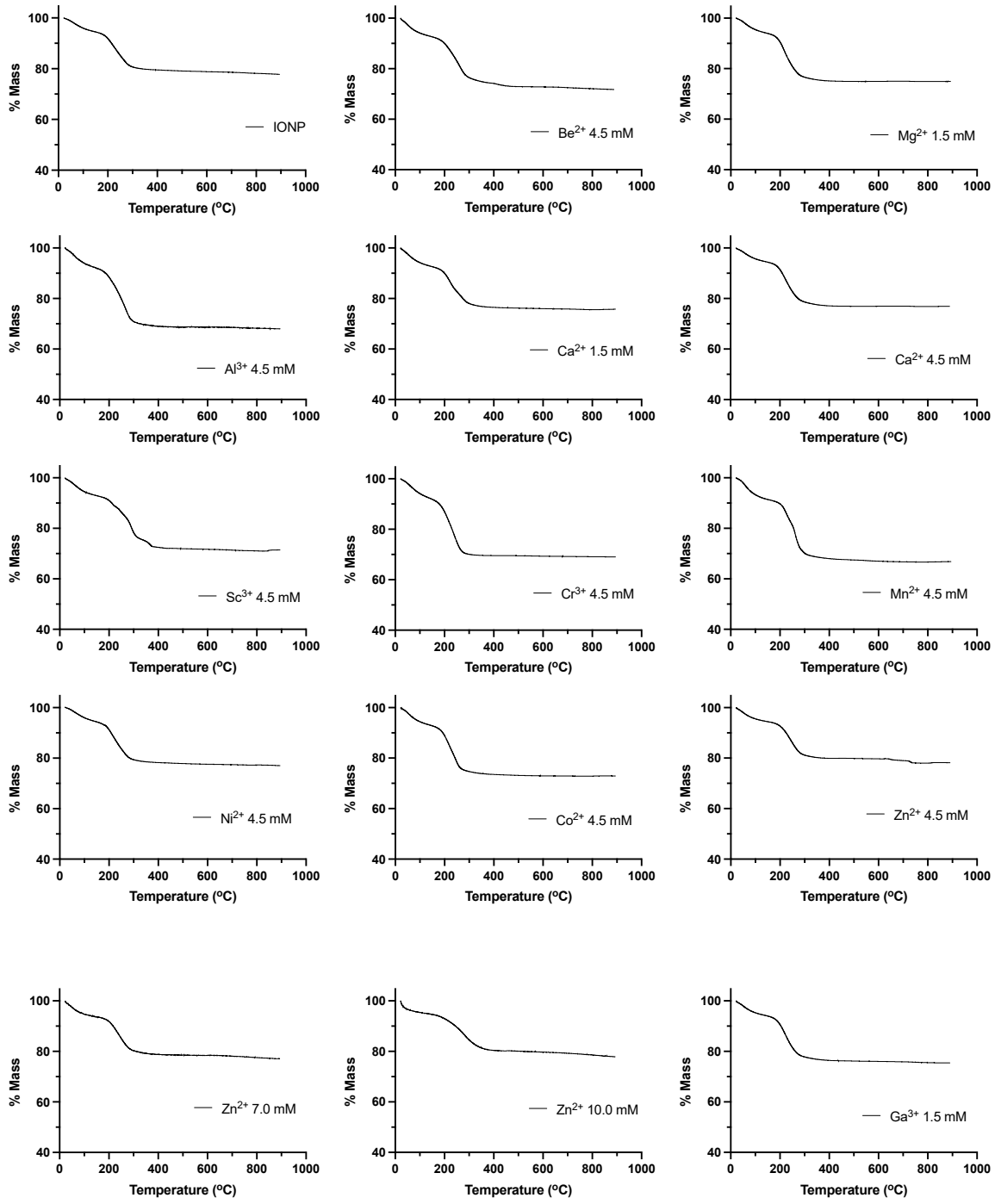

Figure S2. Thermogravimetric curves for metal-doped IONP.

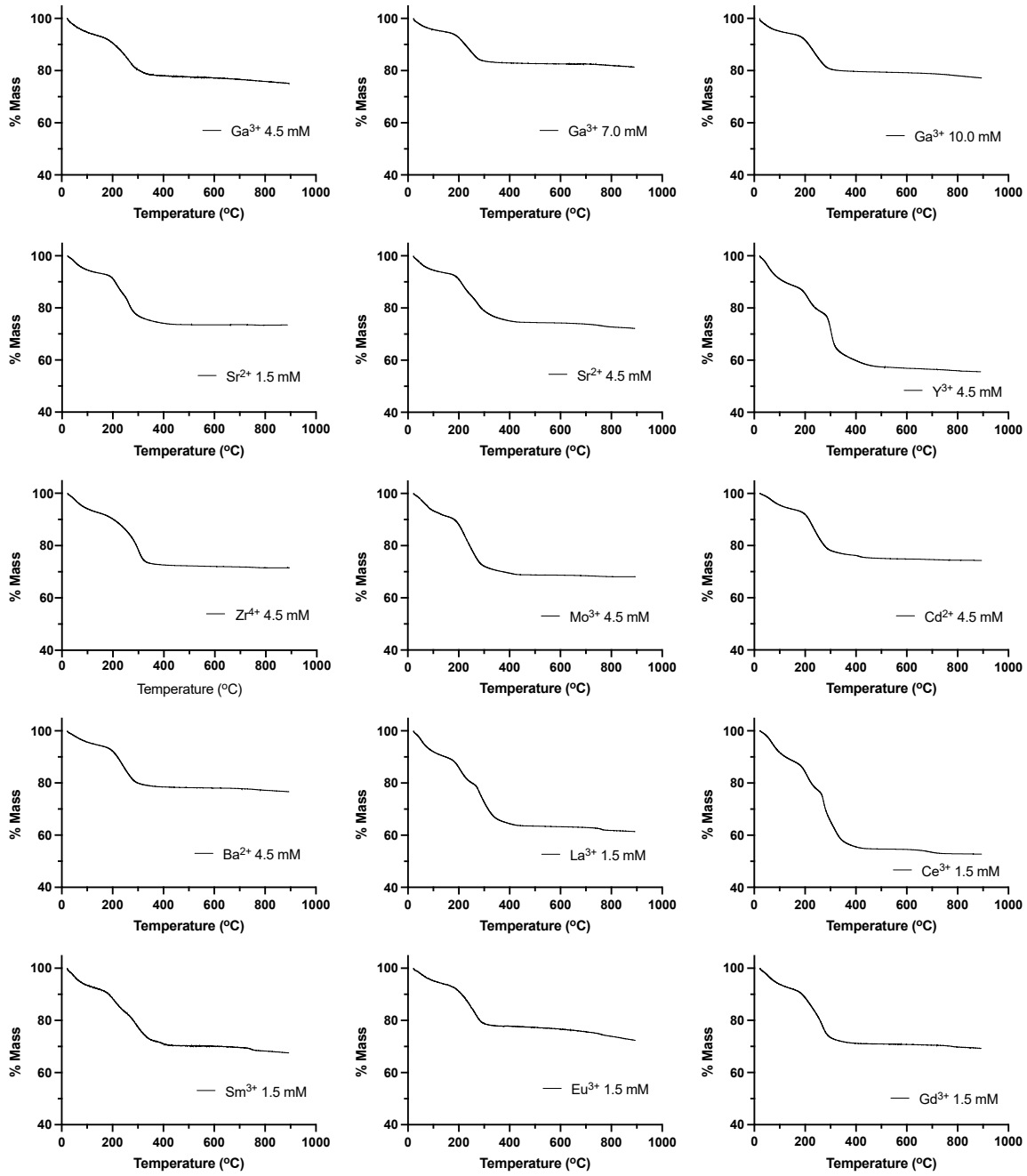

Figure S2. (Cont.)

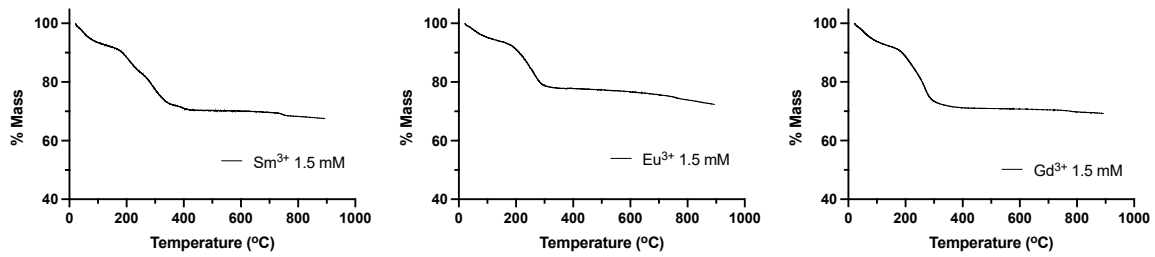

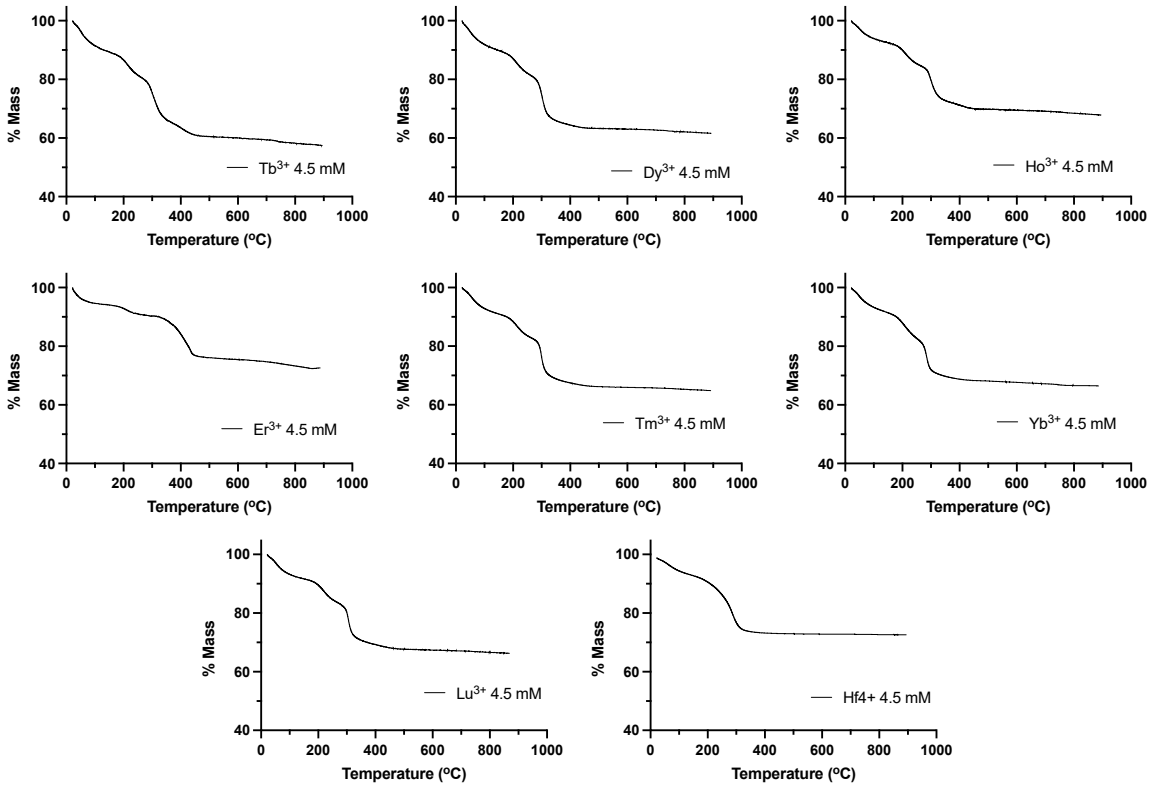

Figure S2. (Cont.)

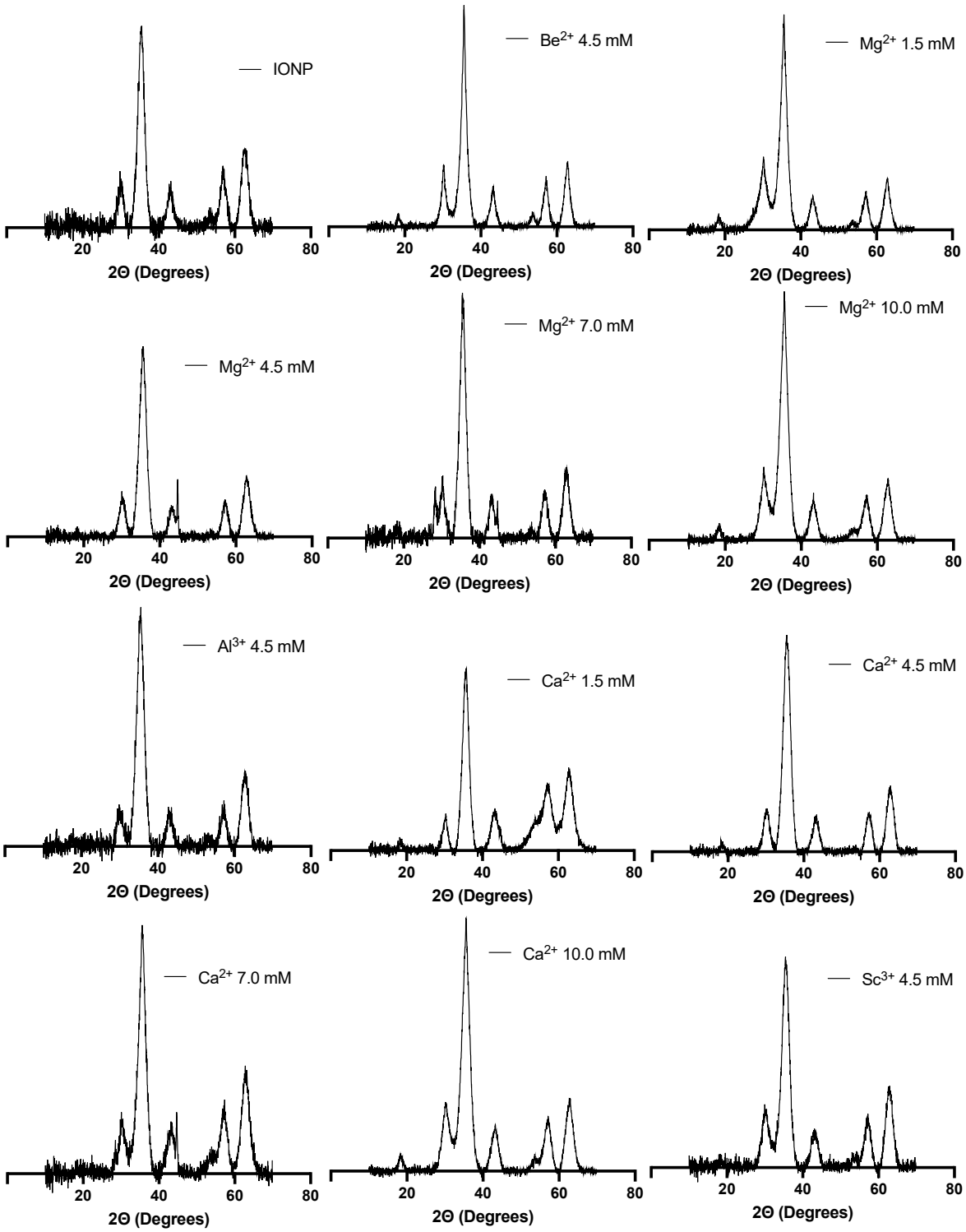

Figure S3. XRD spectrum for different metal-doped IONP.

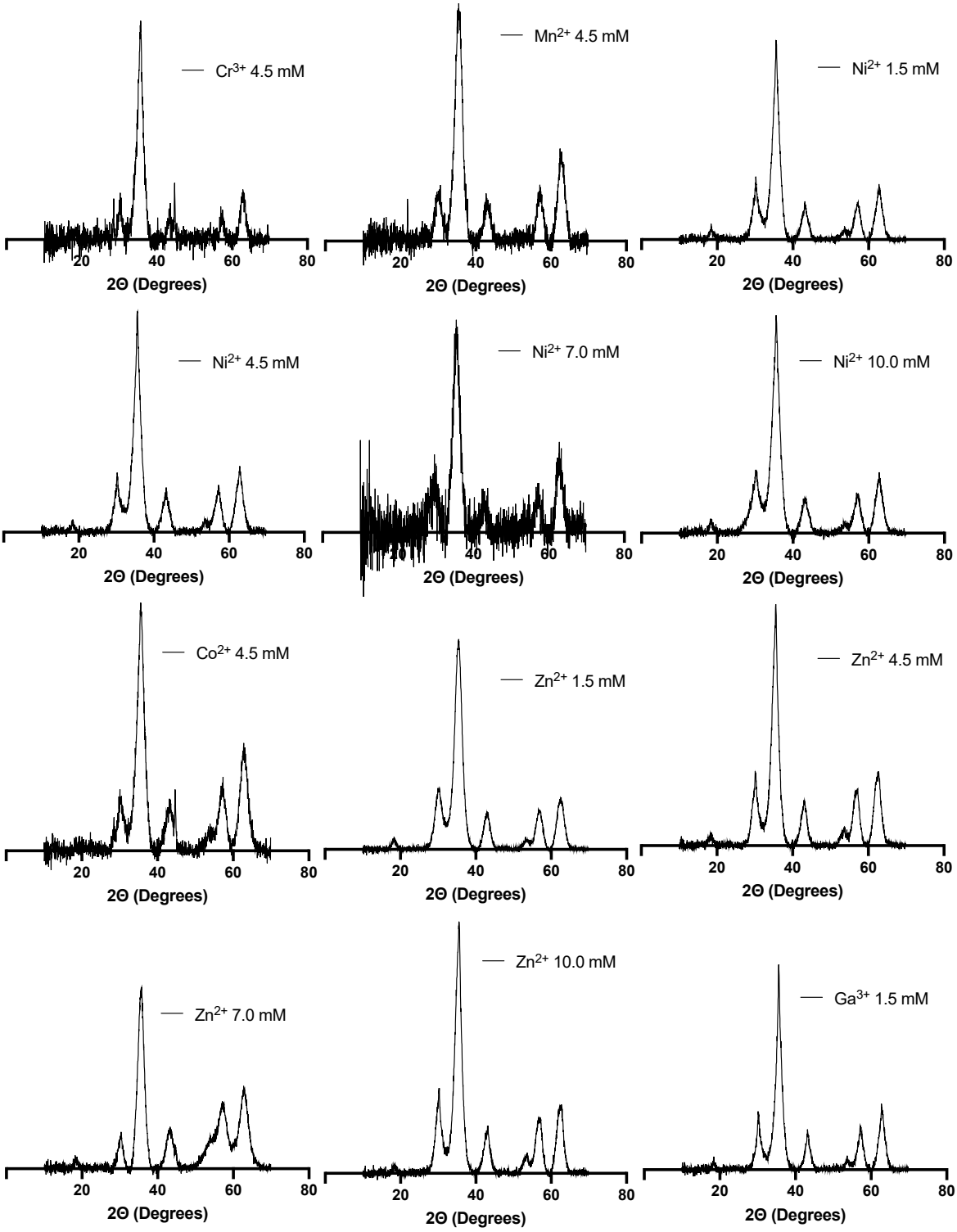

Figure S3. (cont.)

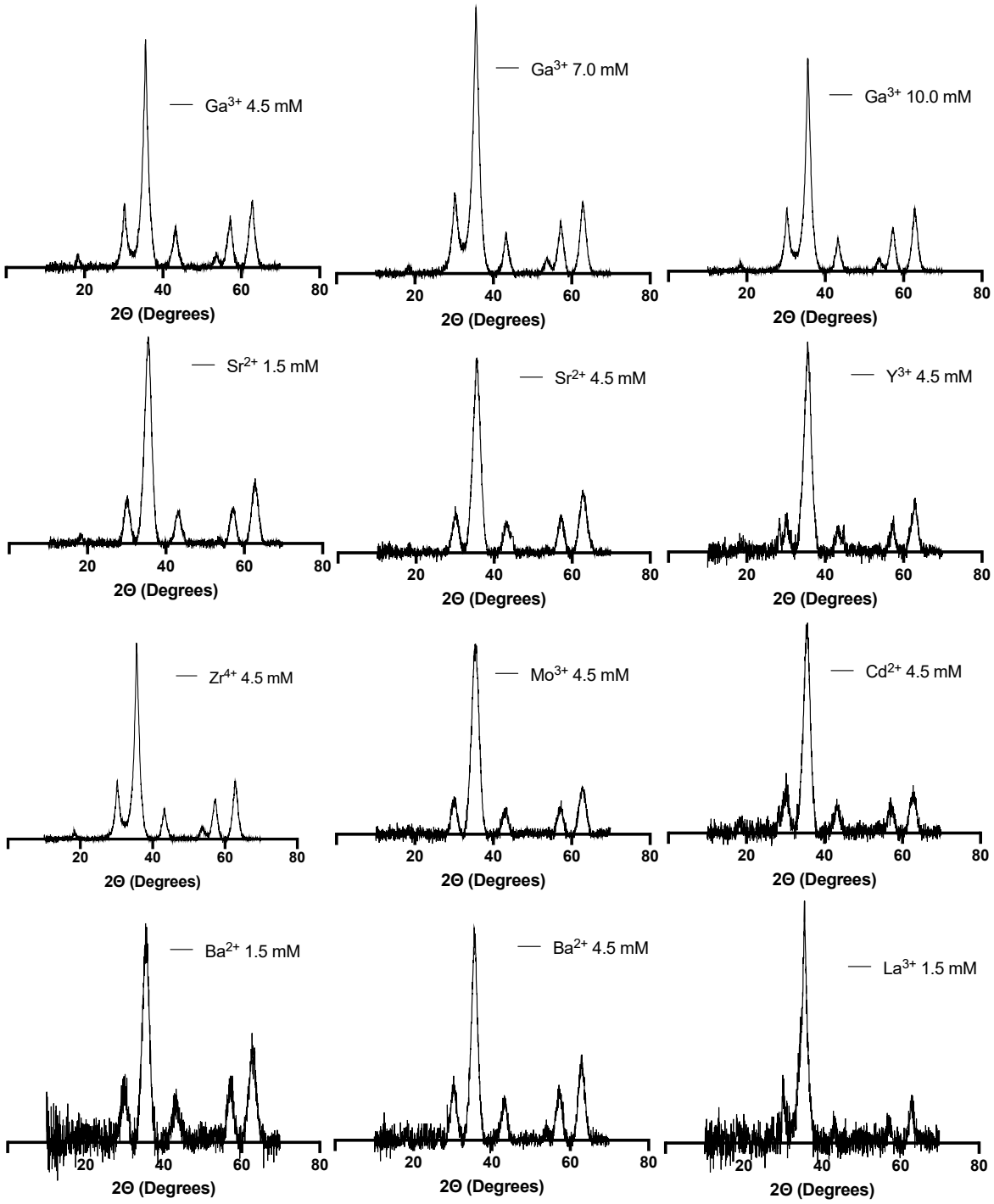

Figure S3. (cont.)

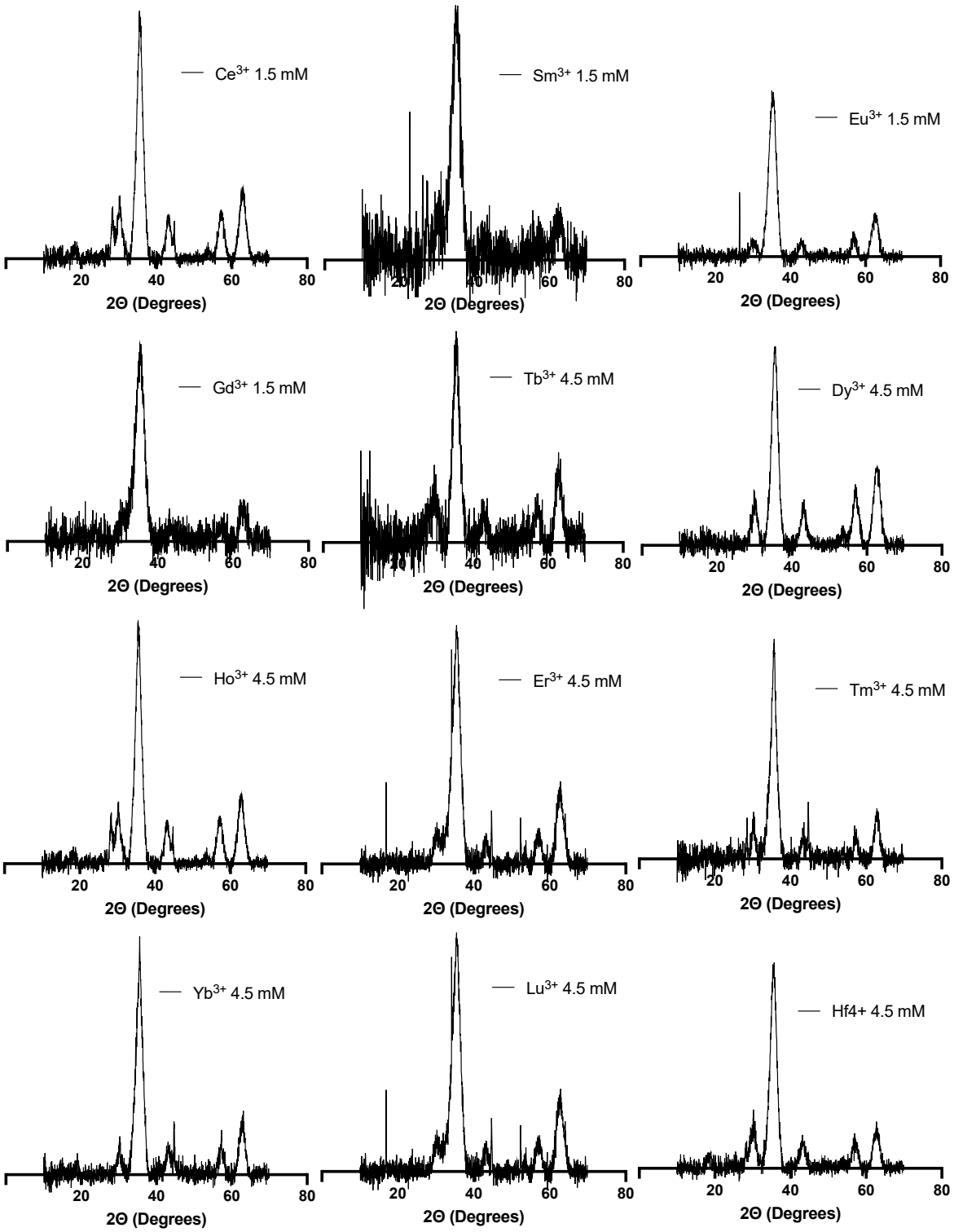

Figure S3. (cont.)

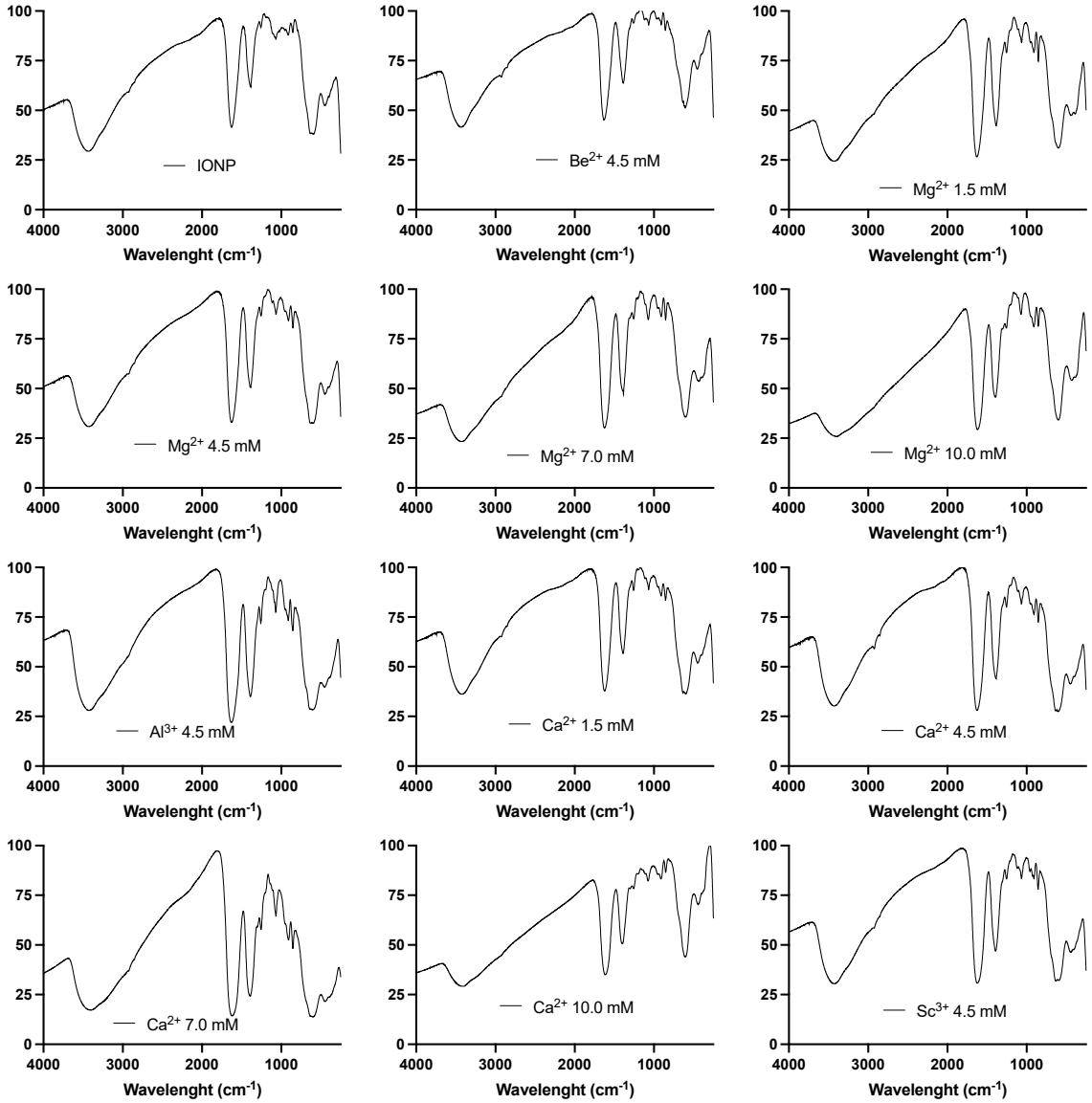

Figure S4. Fourier transform infrared (FTIR) spectra of metal-doped IONP.

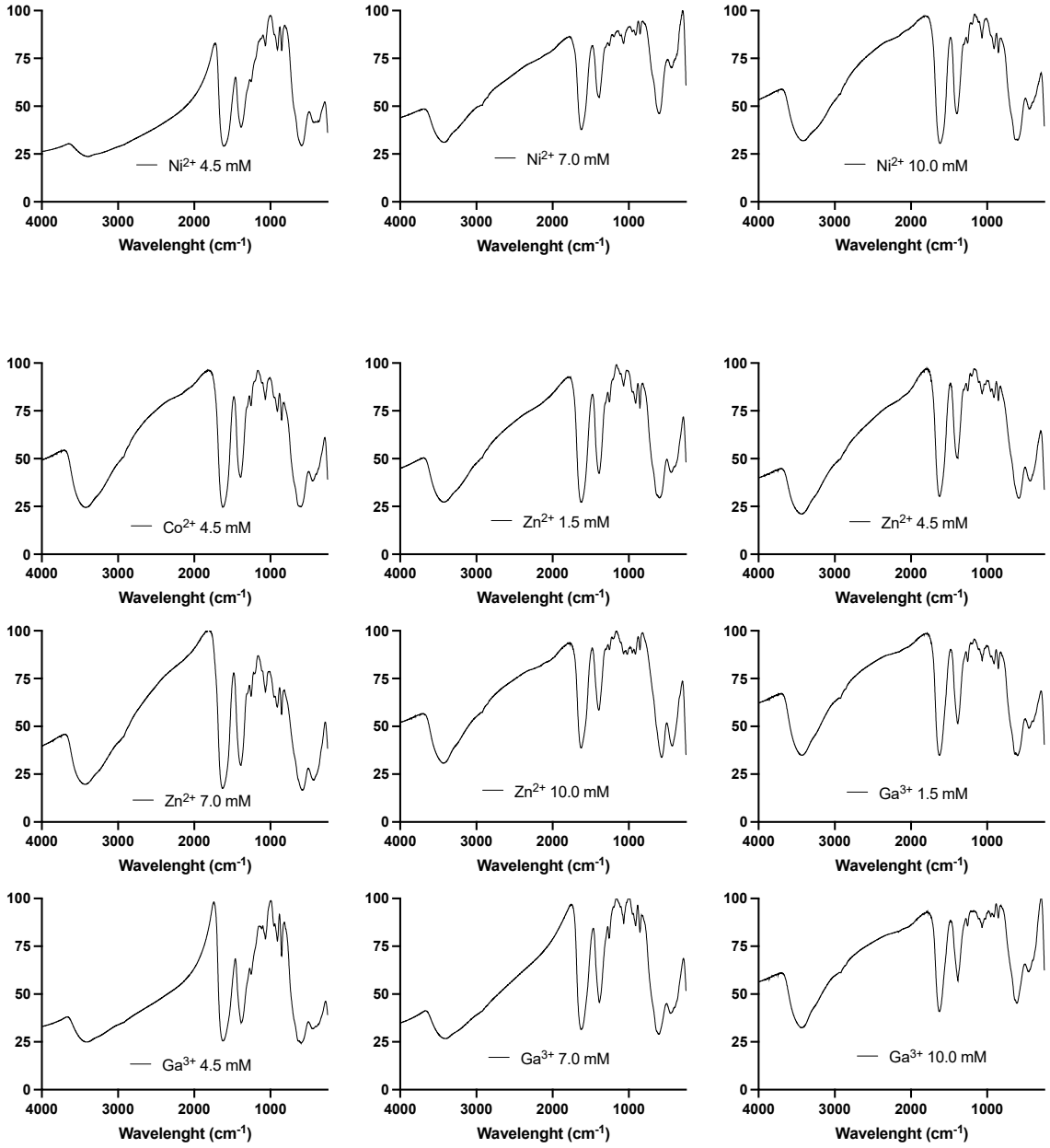

Figure S4. (Cont.)

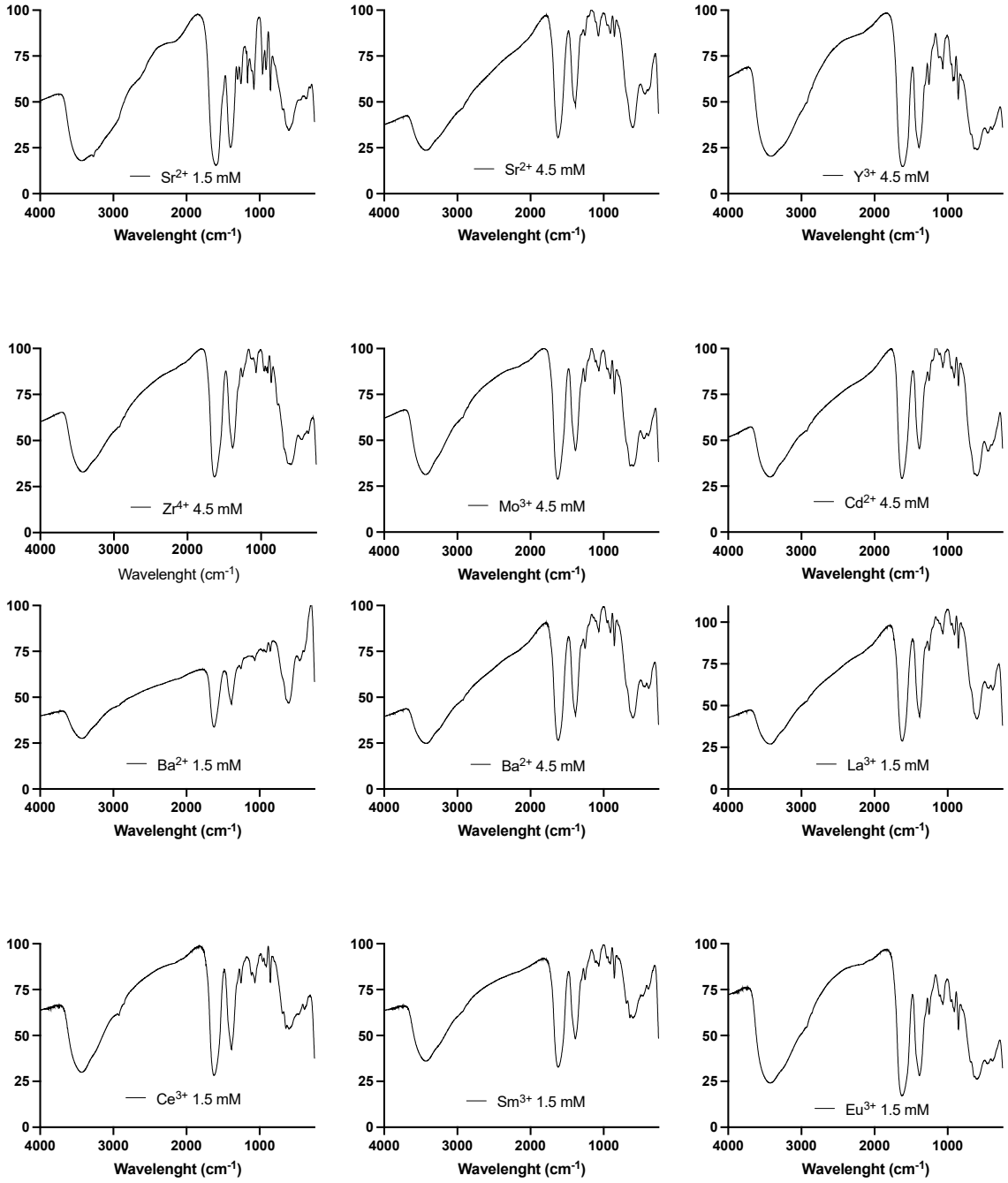

Figure S4. (Cont.)

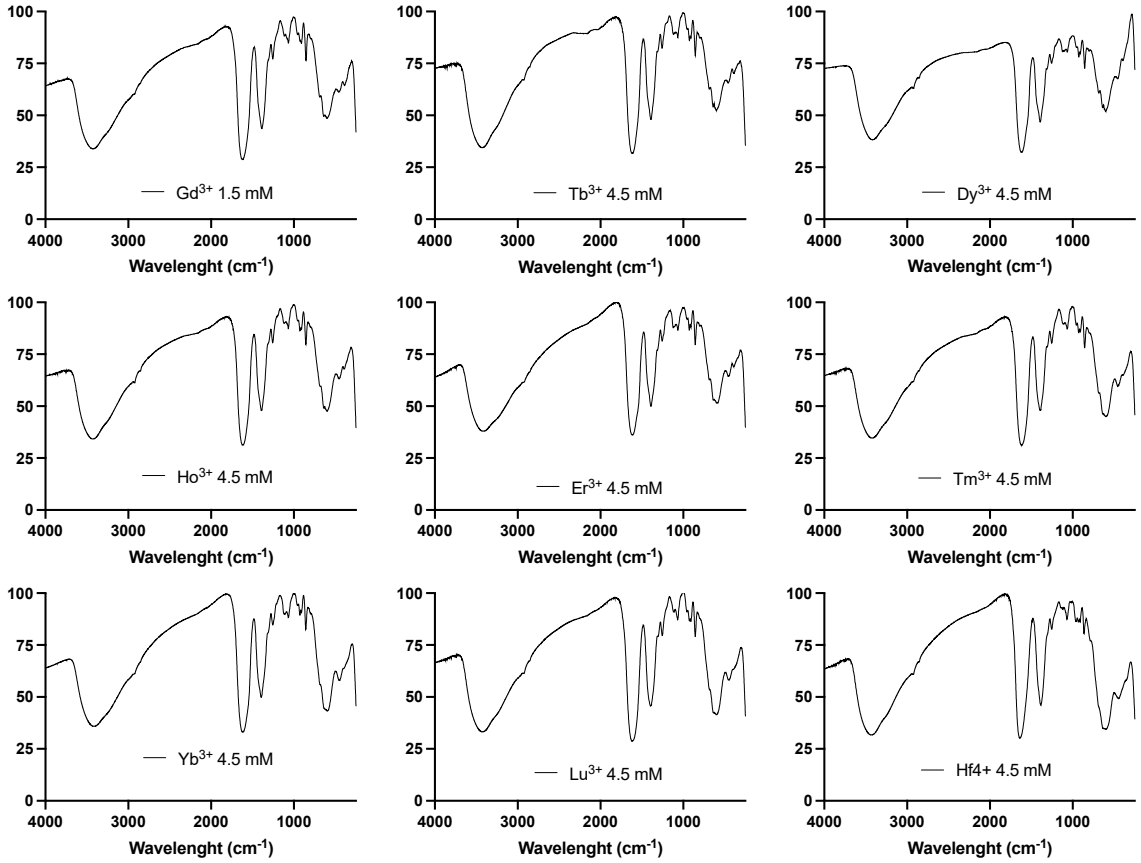

Figure S4. (Cont.)

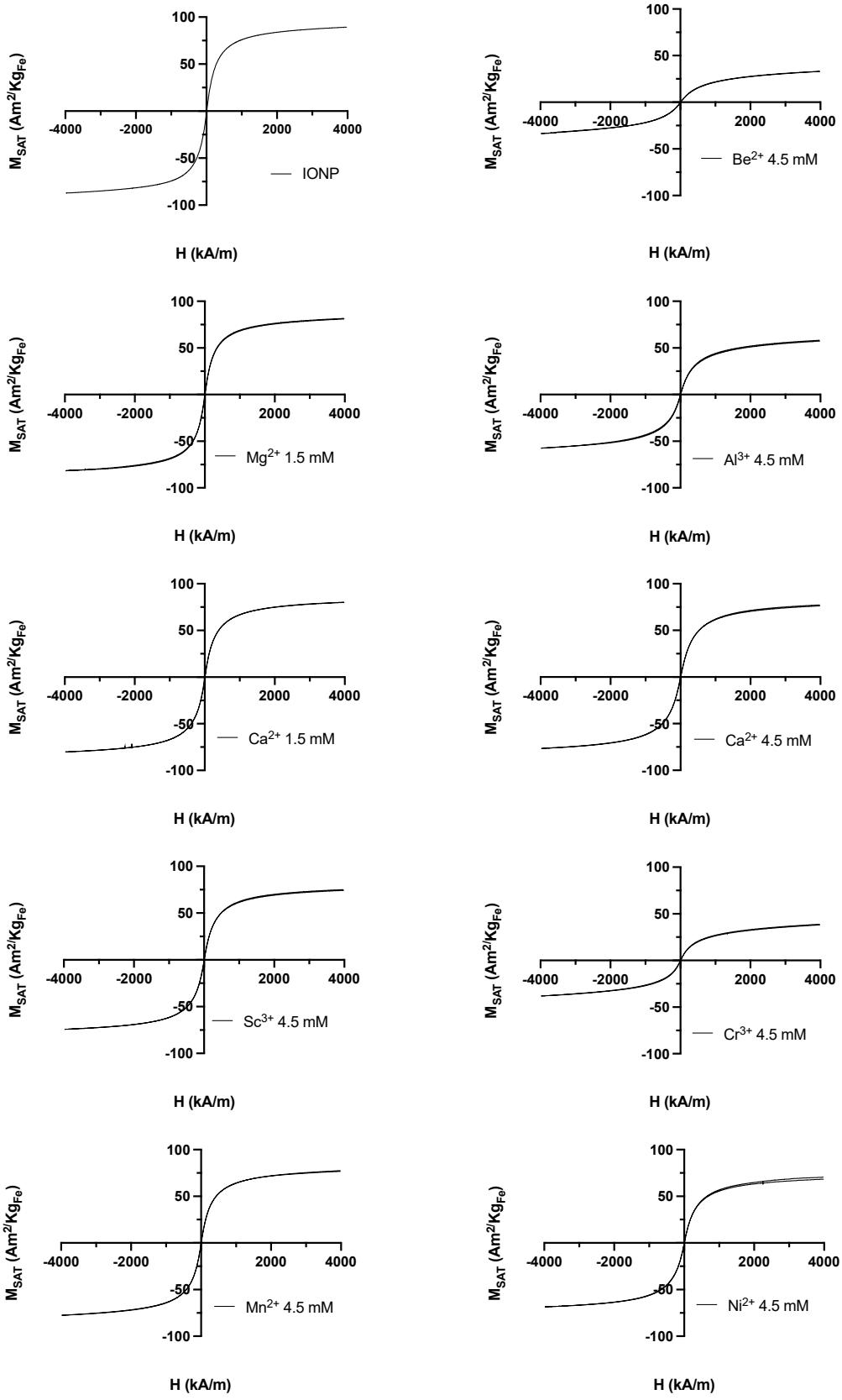

Figure S5. Magnetization curves at 298 K for the different metal-doped IONP.

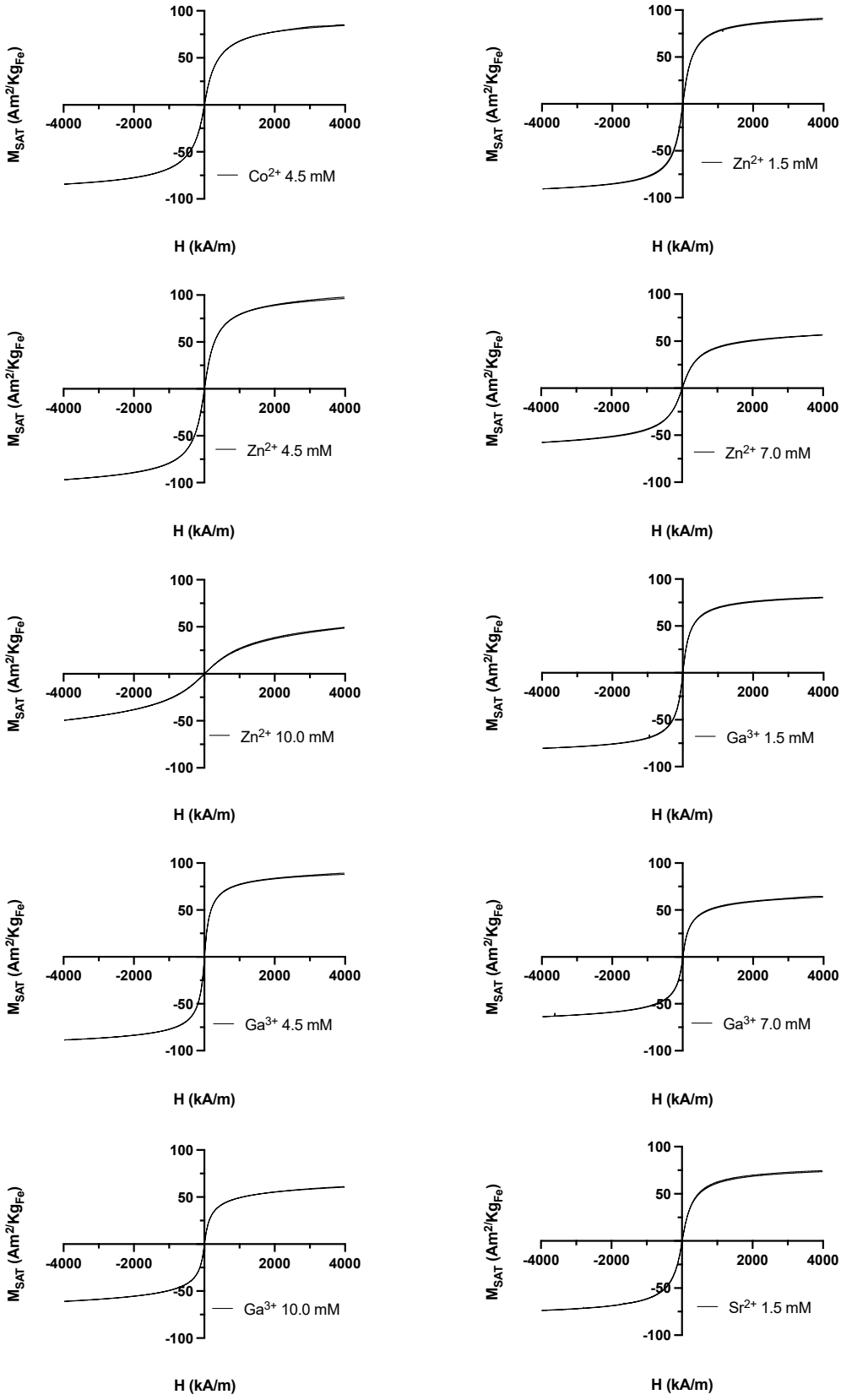

Figure S5. (cont.)

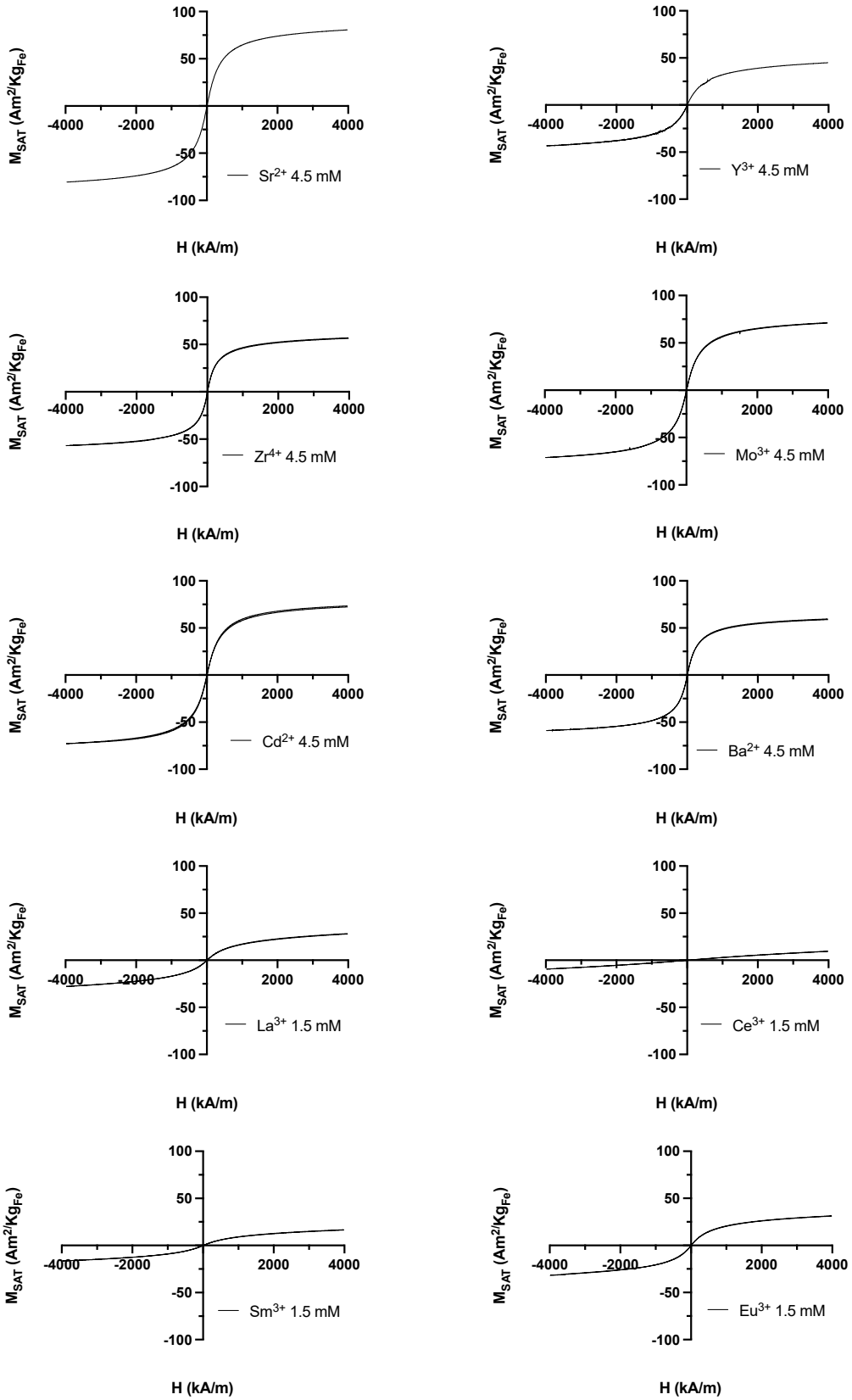

Figure S5. (cont.)

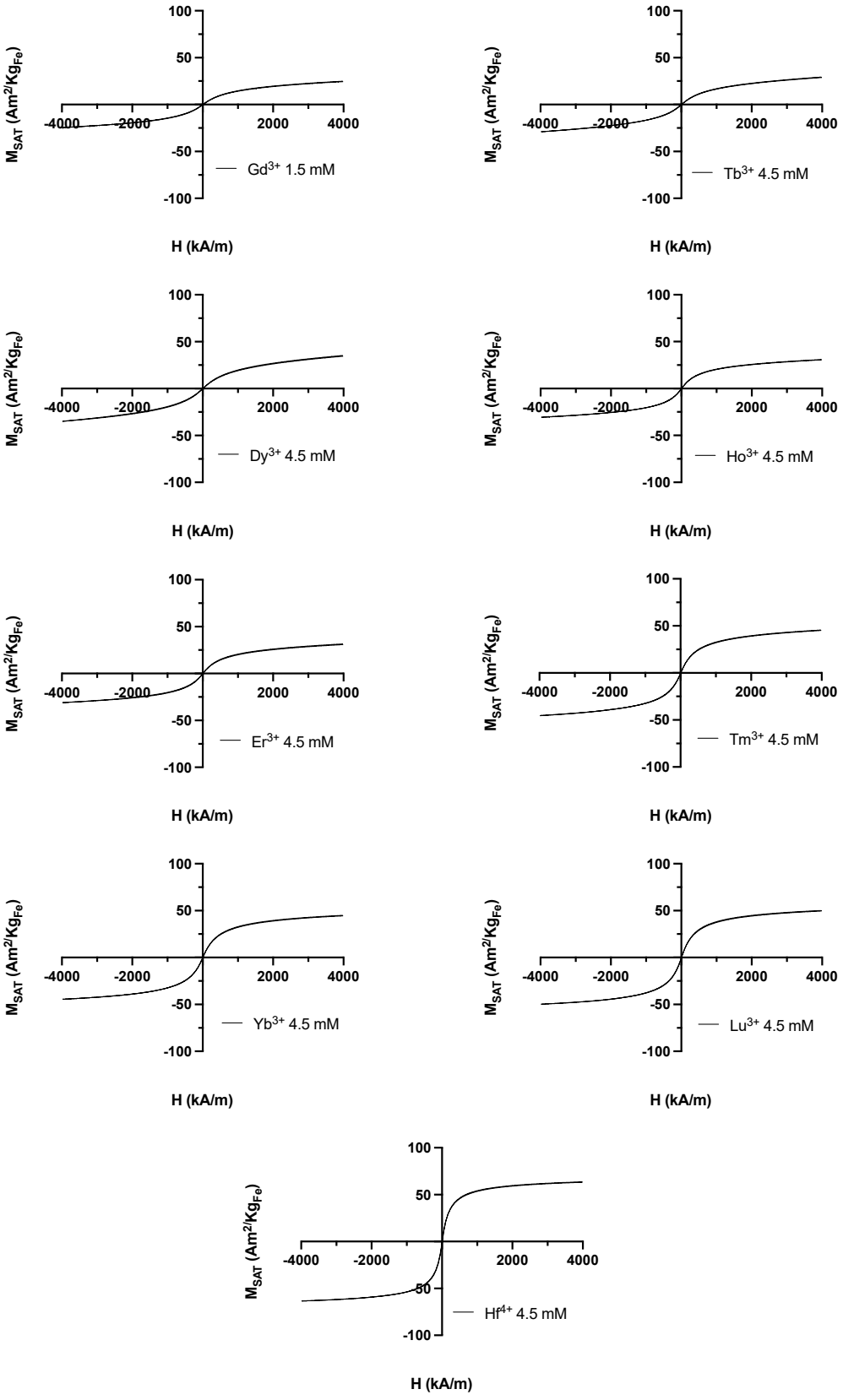

Figure S5. (cont.)

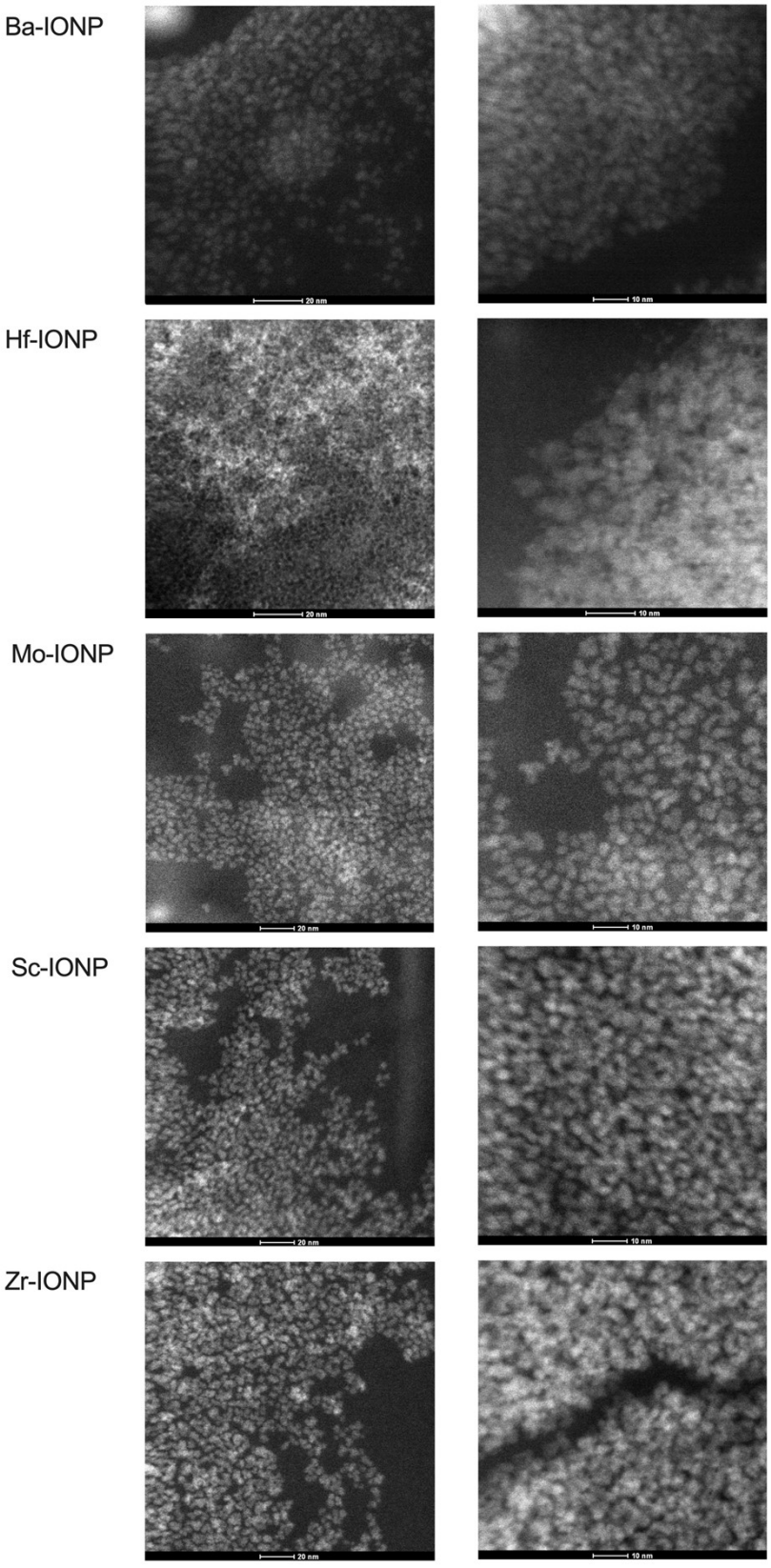

Figure S6. Selected STEM-HAADf images for Ba, Hf, Mo, Sc and Zr doped IONP.

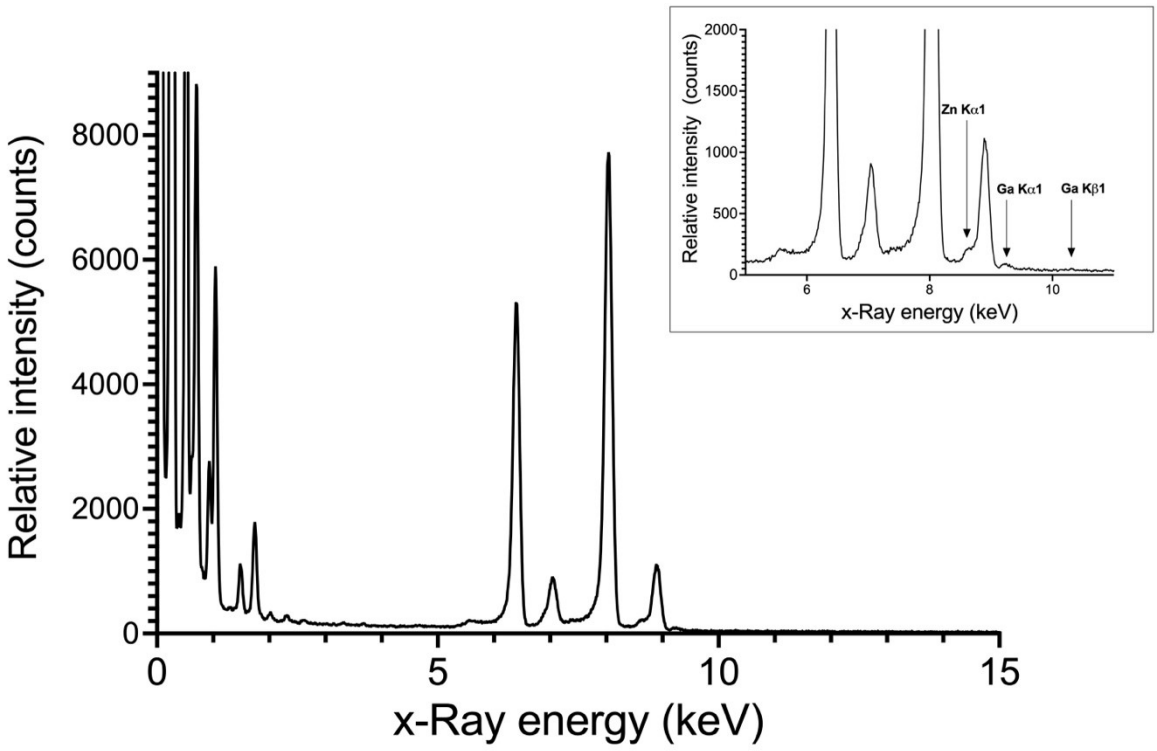

Figure S7. EDS spectrum of GaZn-IONP.

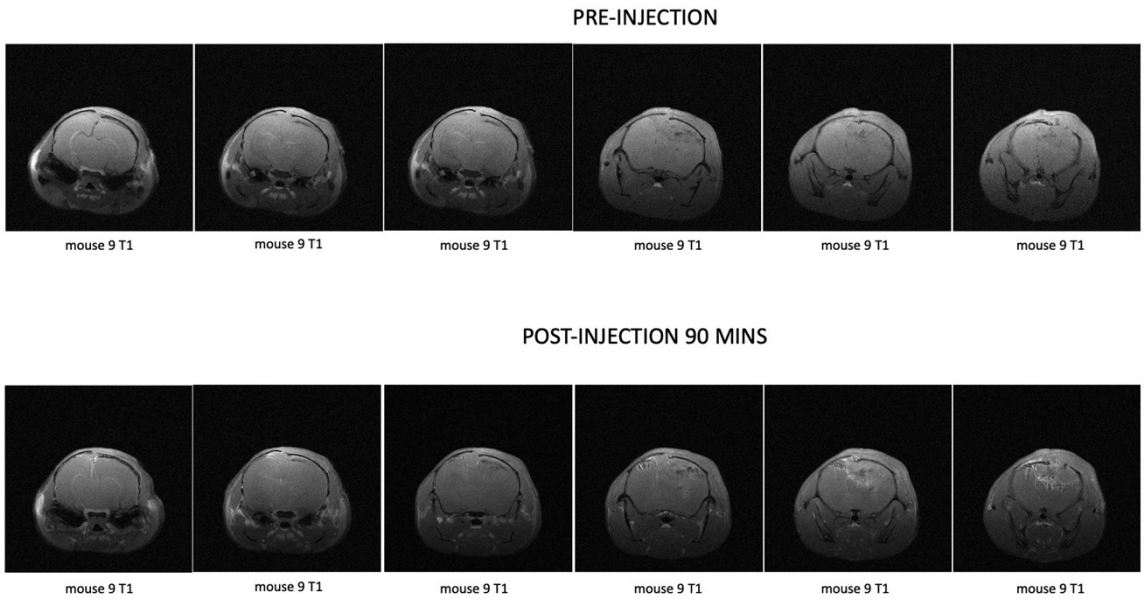

Figure S8. T_1 images for baseline and 90 min after the injection of 0.06 mmol Fe/kg of GaZn-IONP.

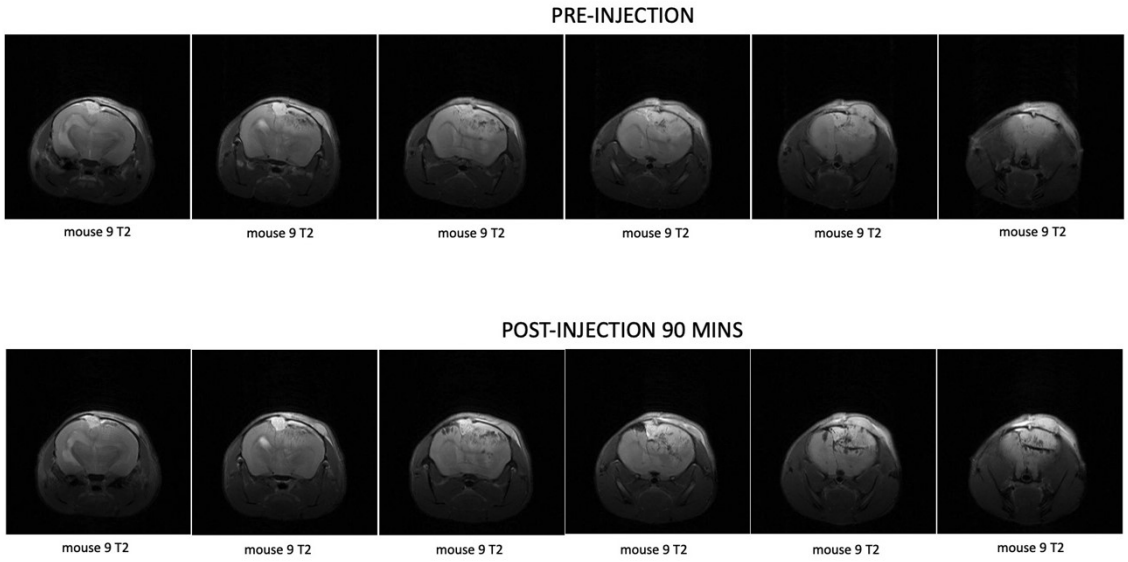

Figure S9. T_2 images for baseline and 90 min after the injection of 0.06 mmol Fe/kg of GaZn-IONP.

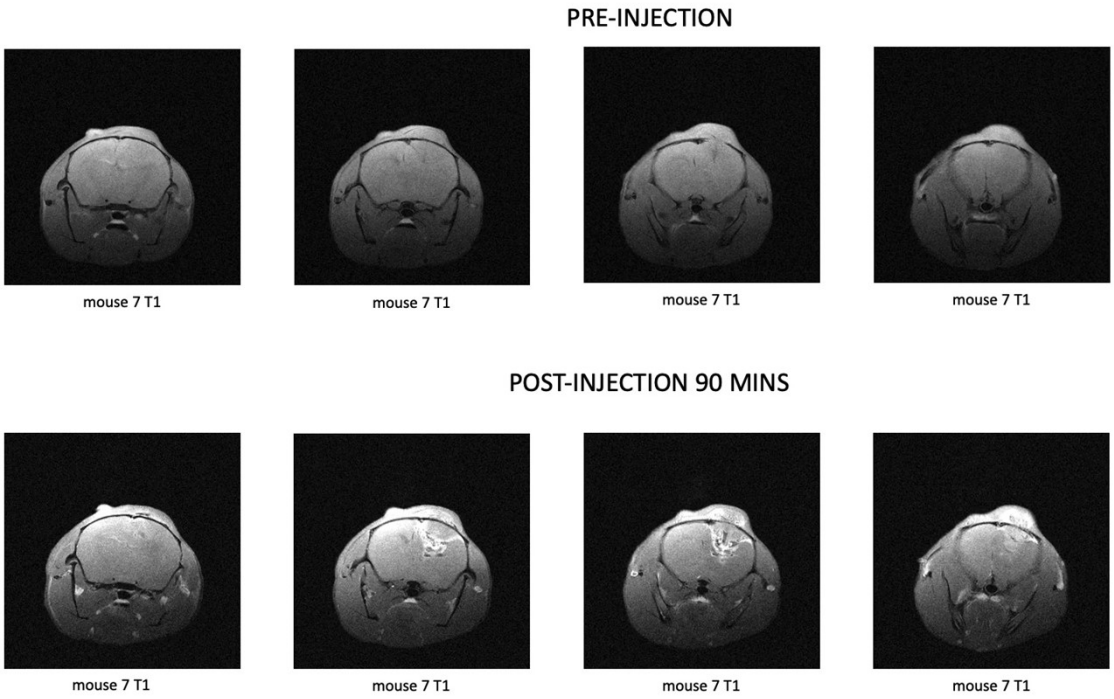

Figure S10. T_1 images for baseline and 90 min after the injection of 0.06 mmol Fe/kg of GaZn-IONP.